

Ultra-broadband and wide-angle reflective terahertz polarization conversion metasurface based on topological optimization

Ya-Jie Zhang(张亚杰), Chao-Long Li(李潮龙), Jia-Qi Luan(栾迦淇), Ming Zhao(赵茗), Ding-Shan Gao(郜定山), and Pei-Li Li(李培丽)

Citation: Chin. Phys. B, 2024, 33 (**10**): 104210. DOI: 10.1088/1674-1056/ad5d91
Journal homepage: http://cpb.iphy.ac.cn; http://iopscience.iop.org/cpb

What follows is a list of articles you may be interested in

Enhancing the Goos-Hänchen shift based on quasi-bound states in the continuum through material asymmetric dielectric compound gratings

Xiaowei Jiang(江孝伟), Bin Fang(方彬), and Chunlian Zhan(占春连)
Chin. Phys. B, 2024, 33 (**3**): 034206. DOI: 10.1088/1674-1056/acf661

Giant and controllable Goos—Hänchen shift of a reflective beam off a hyperbolic metasurface of polar crystals

Tian Xue(薛天), Yu-Bo Li(李宇博), Hao-Yuan Song(宋浩元), Xiang-Guang Wang(王相光), Qiang Zhang(张强), Shu-Fang Fu(付淑芳), Sheng Zhou(周胜), and Xuan-Zhang Wang(王选章)
Chin. Phys. B, 2024, 33 (**1**): 014207. DOI: 10.1088/1674-1056/acdac2

A 1-bit electronically reconfigurable beam steerable metasurface reflectarray with multiple polarization manipulations

Yan Shi(史琰), Xi-Ya Xu(徐茜雅), Shao-Ze Wang(王少泽), Wen-Yue Wei(魏文岳), and Quan-Wei Wu(武全伟)
Chin. Phys. B, 2024, 33 (**1**): 014201. DOI: 10.1088/1674-1056/acfa8a

Real-time and high-transmission middle-infrared optical imaging system based on a pixel-wise metasurface micro-polarization array

Lifeng Ma(马丽凤), Shan Du(杜杉), Jun Chang(常军), Weilin Chen(陈蔚霖), Chuhan Wu(武楚晗), Xinxin Shi(石鑫鑫), Yi Huang(黄翼), Yue Zhong(钟乐), and Quanquan Mu(穆全全)
Chin. Phys. B, 2023, 32 (**8**): 084201. DOI: 10.1088/1674-1056/acaa25

High efficiency and high transmission asymmetric polarization converter with chiral metasurface in visible and near-infrared region

Yuhang Gao(高雨航), Yu Tian(田宇), Qingguo Du(杜庆国), Yuanli Wang(王原丽), Qin Fu(付琴), Qiang Bian(卞强), Zhengying Li(李政颖), Shuai Feng(冯帅), and Fangfang Ren(任芳芳)
Chin. Phys. B, 2023, 32 (**7**): 074201. DOI: 10.1088/1674-1056/acb9eb

---

Ultra-broadband and wide-angle reflective terahertz polarization conversion metasurface based on topological optimization

Ya-Jie Zhang(张亚杰)[1], Chao-Long Li(李潮龙)[1], Jia-Qi Luan(栾迦淇)[1], Ming Zhao(赵茗)[2], Ding-Shan Gao(郜定山)[2], and Pei-Li Li(李培丽)[1,†]

[1] *Faculty of Electrical and Optical Engineering, Nanjing University of Posts and Communications, Nanjing* 210023, *China*
[2] *Wuhan National Laboratory for Optoelectronics and School of Physics, Huazhong University of Science and Technology, Wuhan* 430074, *China*

(Received 23 April 2024; revised manuscript received 13 June 2024; accepted manuscript online 2 July 2024)

Terahertz polarization conversion devices have significant potential applications in various fields such as terahertz imaging and spectroscopy. In this paper, we utilize genetic algorithms to topologically optimize the metasurface unit cells and design a reflective linear polarization conversion metasurface with ultra-broadband and wide-angle characteristics. By partitioning the metallic pattern layer into quadrants, the encoding length is effectively reduced, resulting in a shorter optimization time. The research results indicate that the converter possesses a polarization conversion efficiency ratio higher than 90% and a relative bandwidth ratio of 125% in a range of 0.231–0.995 THz. Meanwhile, it can maintain excellent polarization conversion properties when the incident angle of terahertz waves is less than 45° and the polarization angle is less than 15°, demonstrating excellent practicality. New insights are provided for the design of terahertz wide-angle ultra-wideband polarization conversion devices, and the proposed metasurfce has potential applications in terahertz polarization imaging, spectroscopy and communication fields.

Keywords: metasurface, polarization conversion, topology optimization, ultra-broadband

PACS: 42.25.Bs, 41.20.Jb **DOI:** 10.1088/1674-1056/ad5d91

1. Introduction

Terahertz (THz) waves have potential applications in fields such as sensing, communication and imaging technologies due to their unique electromagnetic characteristics. In recent years, the emergence of efficient THz emitters and sensitive detectors has opened up new avenues for exploring THz applications. THz polarization conversion devices have broad application prospects and have been extensively researched in THz imaging, spectroscopy and THz communication fields. Traditional methods for modulating polarization involve the use of birefringent materials, gratings or birefringent crystals with delay effects. However, these polarization modulation devices typically suffer from drawbacks such as a large volume, a narrow operating bandwidth and high loss.[1–3]

Metasurfaces have the advantages of flexible manipulation of electromagnetic waves, compact size and ease of integration, providing new avenues for modulating the polarization states of THz waves. According to their different operating modes, THz metasurface polarization modulation devices can be categorized into reflective and transmissive types, each having distinct application scenarios. Transmissive polarization conversion metasurfaces have unique applications in holography and imaging. Transmissive polarization metasurfaces can achieve a maximum relative bandwidth of polarization conversion of up to 135%, and mostly consist of multi-layered metallic resonant structures composed of two orthogonal metal grids.[4–9] Compared with transmissive polarization conversion metasurfaces, reflective polarization conversion metasurfaces have important advantages in terms of energy efficiency and a wide range of applications in fields such as radar cross-section reduction[10,11] and stealth suits.[12] Reflective polarization metasurfaces mainly comprise metallic pattern layers, dielectric layers and metal backplanes, but relative operational bandwidths of 120% are difficult to exceed.

A reflective metasurface consisting of T-shaped resonant layers was proposed by Ako *et al.*;[13] it achieved a polarization conversion efficiency above 80% in the 0.31–1.05 THz range and maintained favorable polarization conversion performance within a 45° incident angle. A reflective metasurface composed of crescent-shaped resonant layers was proposed by Gandhi *et al.*;[14] this achieved a polarization conversion efficiency above 90% in the 0.64–1.47 THz range. It could maintain a favorable polarization conversion performance when the incident angle was less than 30°. Xu *et al.* proposed a reflective metasurface composed of dual-split-ring resonators,[15] which achieved polarization conversion in the range of 0.47–1.88 THz. The results showed that the conversion performance of this device was good for incidence angles ranging from 0° to 20°. A dumbbell shaped resonant layer was proposed by Nagini and Chandu.[16] This achieved a line-polarized transition at 1.76–4.26 THz and the conversion efficiency was greater than 95%. Bai *et al.*[17] suggested a reflective metasurface combining C- and T-shaped resonant layers. This achieved polarization conversion efficiency above 99%

†Corresponding author. E-mail: lipl@njupt.edu.cn

© 2024 Chinese Physical Society and IOP Publishing Ltd

in the 5–10 THz range. The polarizer exhibited an excellent angular stability up to 30° of incidence. Zhao *et al.*[18] described a fully dielectric reflective metasurface that achieved a linear polarization conversion efficiency greater than 95% in the 1.21–1.92 THz range.

In summary, there are certain limitations to the operational bandwidth of polarization conversion, and a significant reduction in the operational bandwidth at high conversion efficiency occurs under large-angle incidence. The wide-angle characteristics of polarization conversion are important performance indicators in practical engineering. The smaller the dependence on the incident angle, the better the practicality in practical measurement and application. Consequently, research into ultra-broadband and wide-angle reflective polarization conversion metasurfaces has particular significance.

In recent years, THz polarization modulation devices have been gradually trending towards multifunctionality and bandwidth tunability. This mainly includes flexible switching of multiple functions,[19–23] polarization conversion throughout the space[24] and switching of the working bandwidth[25,26] by using adjustable materials such as VO_2, graphene and Dirac materials. Although metasurfaces utilizing tunable materials possess certain advantages in terms of functional diversity and tunability, they often struggle to achieve relative bandwidths exceeding 100% in the THz frequency range. Additionally, both the fabrication and external control of metasurfaces pose certain difficulties.

Ultra-broadband and highly efficient polarization conversion devices can be realized through the design of the metallic pattern layer of metasurfaces. Compared with basic pattern and structural parameter optimization, topological optimization enhances design flexibility, thereby achieving better performance. Sui *et al.*[27] used a genetic algorithm to topologically optimize a microwave polarization converter, which effectively widened the relative bandwidth of polarization conversion up to 116%. However, the conversion efficiency could not consistently exceed 90% across the entire operational frequency band. A topological optimization method[28] was employed to reverse-engineer a wide-angle polarization metasurface in the microwave band, achieving a relative bandwidth of approximately 117%. However, the optimization process was rather intricate, and to maximize bandwidth enhancement the dielectric material was air, which had certain limitations.

In this paper, we propose a reflective THz ultra-broadband and wide-angle polarization conversion metasurface based on topological optimization. The metasurface unit cell structure consists of a metallic pattern layer, upper and lower dielectric layers and a metallic substrate. By partitioning the metallic pattern layer into quadrants and employing genetic algorithms for inverse design of the metasurface metallic pattern layer and structural parameters, the encoding length is effectively reduced, resulting in a shorter optimization time. The ultra-broadband polarization conversion mechanism of the designed metasurface is explained through theoretical analysis and surface current distribution. Additionally, the polarization conversion characteristics under oblique incidence and different polarization angles are simulated and analyzed.

2. Theoretical analysis of linear polarization conversion

Based on electromagnetic field theory, we analyze the principle of linear polarization conversion of electromagnetic waves incident on the metasurface. As shown in Fig. 1(a), the incident y-polarized electromagnetic wave propagates along the negative z-axis. The electric ($\boldsymbol{E}$) and magnetic ($\boldsymbol{H}$) fields are directed along the y-axis and x-axis, respectively. The x–y axes are rotated counterclockwise around the z-axis by 45° to obtain the u–v axes. The electric field vector of the incident y-polarized wave can be decomposed into two components along the u and v axes. When $z = 0$, the incident and reflected electric fields are respectively represented as

$$\boldsymbol{E}_{\rm i} = \boldsymbol{e}_u E_{{\rm i}u} + \boldsymbol{e}_v E_{{\rm i}v}, \tag{1}$$

$$\boldsymbol{E}_{\rm r} = \boldsymbol{e}_u E_{{\rm r}u}\cos(\omega t + \varphi_u) + \boldsymbol{e}_v E_{{\rm r}v}\cos(\omega t + \varphi_v), \tag{2}$$

where $\boldsymbol{e}_u$ and $\boldsymbol{e}_v$ represent unit vectors along the u and v axes, respectively, $E_{{\rm i}u}$ and $E_{{\rm i}v}$ are the magnitudes of the incident electric field along the u and v axes, respectively, $E_{{\rm r}u}$ and $E_{{\rm r}v}$ are the magnitudes of the reflected electric field along the u and v axes, respectively, and φ_u and φ_v represent the reflection phases along the u and v axes, respectively. The phase difference between φ_u and φ_v is denoted as $\Delta\varphi = \varphi_u - \varphi_v$. When $\Delta\varphi = \pi$ and $E_{{\rm r}u}/E_{{\rm r}v} = E_{{\rm i}u}/E_{{\rm i}v}$, $\boldsymbol{E}_{\rm r} = -\boldsymbol{e}_u E_{{\rm r}u}\cos(\omega t + \varphi_u) + \boldsymbol{e}_v E_{{\rm r}v}\cos(\omega t + \varphi_v)$, the polarization direction of the synthesized electromagnetic wave undergoes a 90° rotation, resulting in cross-polarization conversion after reflection, as shown in Fig. 2(b). The polarization conversion efficiency is evaluated using the polarization conversion ratio (PCR), typically expressed in reflection mode as

$$\mathrm{PCR} = \frac{r_{xy}^2}{r_{xy}^2 + r_{yy}^2}, \tag{3}$$

where r is the reflection coefficient, and r_{xy} and r_{yy} correspond to the cross-polarization reflection coefficient and co-polarization reflection coefficient, respectively. Additionally, the relative operating bandwidth (FBW) is defined as

$$\mathrm{FBW} = 2 \times \frac{f_1 - f_2}{f_1 + f_2}, \tag{4}$$

where f_1 and f_2 correspond to the upper and lower limits of the operating frequency band for polarization conversion.

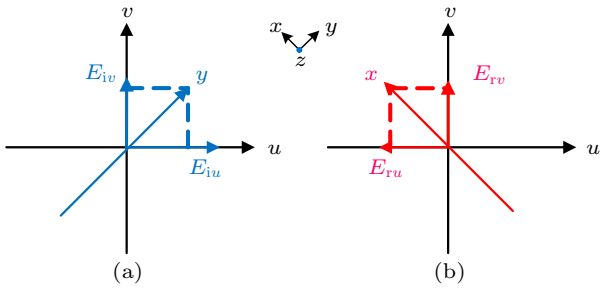


Fig. 1. Schematic of (a) *y*-polarized incident electromagnetic wave and (b) *x*-polarized reflected electromagnetic wave.

3. Topological optimization of the unit structure

The metasurface unit structure designed in this study consists of a metallic pattern layer, upper and lower dielectric layers, and a metallic substrate, as shown in Fig. 2. The dielectric layers utilize cyclo-olefin copolymer (COC),[5] known for its low-loss characteristics in the THz band, serving as supporting and spacer material with a relative dielectric constant of 2.324 and a loss tangent of 0.0007. Both the metallic pattern layer and the metallic substrate are made of copper. The bottom of the metasurface is a metallic plate, resulting in a transmission coefficient of approximately zero when a plane wave vertically impinges on the metasurface. Due to the low loss of the dielectric material, perfect reflection can theoretically be achieved for incident THz waves.

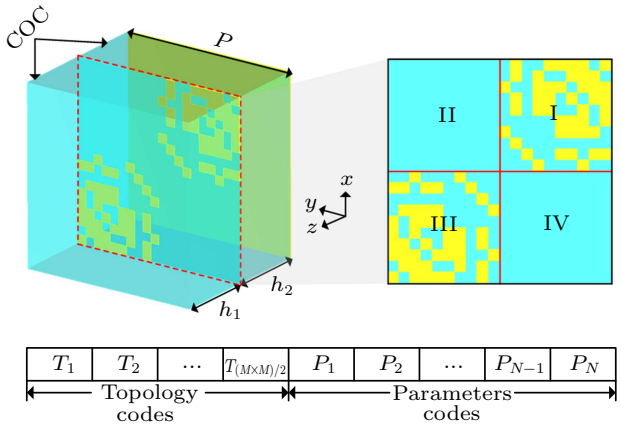


Fig. 2. Design model of the polarization conversion metasurface unit structure.

The essence of electromagnetic wave polarization conversion through a metasurface lies in the electromagnetic resonance between the metallic layers. Therefore, the design of the surface metallic pattern layer is crucial for achieving metasurfaces with highly efficient polarization conversion properties.

In the design of metal patterns for polarization conversion metasurfaces, both axisymmetric structures[27] and encoding length are considered. The better the symmetry, the smaller the encoding length and the greater the possibility of finding the optimal solution within a limited range. In this study, the metallic pattern layer is partitioned into quadrants: the first quadrant is divided into 10×10 pixels with diagonal symmetry, the third quadrant is symmetric to the first quadrant about the center, and the second and fourth quadrants are devoid of metallic pixels. Pixels with and without metal correspond to 1 and 0 in binary, further shortening the length of the topological encoding, corresponding to a maximum sequence of $(M \times M)/2 = 50$. Structural parameter encoding involves encoding the period P, upper COC layer thickness h_1 and lower COC layer thickness h_2 in binary as well. Empirical values for the structural parameters are based on design requirements, as shown in Table 1, where the encoding length corresponds to the maximum binary encoding bits for the structural parameters.

Table 1. Empirical values of the unit structure parameters.

Parameter	Minimum value (μm)	Maximum value (μm)	Coding length
P	50	200	4
h_1	25	100	4
h_2	25	100	4

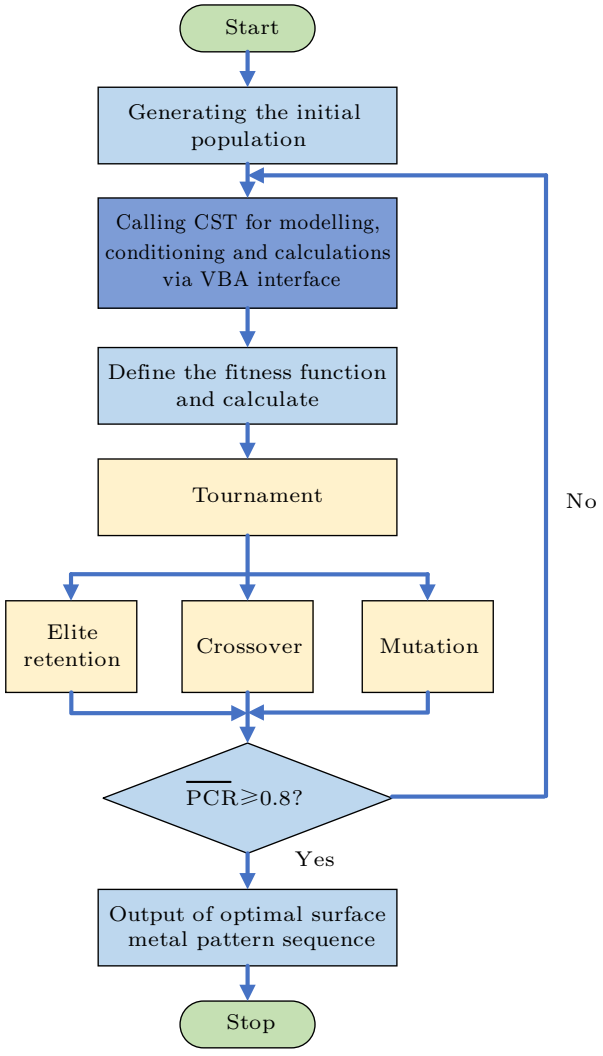


Fig. 3. Flowchart of inverse design of an ultra-wideband polarization conversion metasurface.

Genetic algorithms possess excellent global search capabilities and are widely employed in the design of metasurfaces. In this study, a combined simulation approach using MATLAB

and CST (CST Microwave Studio) is utilized for the topological optimization of the surface metallic pattern. The main program runs the genetic algorithm in MATLAB, which is iteratively called CST for modeling, condition setting and calculation. This iterative process is continued until the target conditions are met, and the optimal metallic pattern sequence is ultimately output. The flowchart of inverse design of ultra-wideband polarization conversion metasurface is illustrated in Fig. 3. The population size is set to 30, and the crossover and mutation probabilities are set to 0.9 and 0.25, respectively.

Taking into account that increasing the incident angle leads to weakening of electromagnetic resonances and thus a general decrease in polarization conversion efficiency, to obtain wide-angle characteristics the plane wave is set to be obliquely incident at 45° during CST full-wave simulation. To maximize the relative bandwidth, the target frequency band is set to $0.1 \le f_1 \le f_2 \le 1$ THz. The fitness function is defined as the average PCR $\overline{\text{PCR}} = \frac{1}{N}\sum_{i=1}^{N} \text{PCR}_i$, where N is the number of sampled frequency points within the operating frequency band.

4. Results and analysis

Figure 4(a) depicts the variation of the fitness function with the number of iterations during the optimization of the genetic algorithm, as well as the evolution of the intermediate topological metal patterns. A, B, C and D are the topological metal pattern layers of 13, 32, 38 and 88 generations in the iterative process, and the corresponding $\overline{\text{PCR}}$ values are 0.144, 0.463, 0.687 and 0.8, respectively. From 0 to 45 generations, the fitness function converges faster and finally converges to the target solution at 88 generations, corresponding to the optimal result D; the coding sequence in its first quadrant is shown in Fig. 4(b).

The optimization process corresponds to the period P, the upper COC thickness h_1 and the lower COC thickness h_2, respectively: P_A, h_{1A} and h_{2A} of 120 μm, 25 μm and 40 μm; P_B, h_{1B} and h_{2B} of 150 μm, 40 μm and 55 μm; P_C, h_{1C} and h_{2C} of 180 μm, 80 μm and 80 μm; and P_D, h_{1D} and h_{2D} of 160 μm, 70 μm and 80 μm. By comparison, it can be clearly seen that the topological pattern structures of A and D are quite different, while C and D have similar structural profiles and the structural parameters converge.

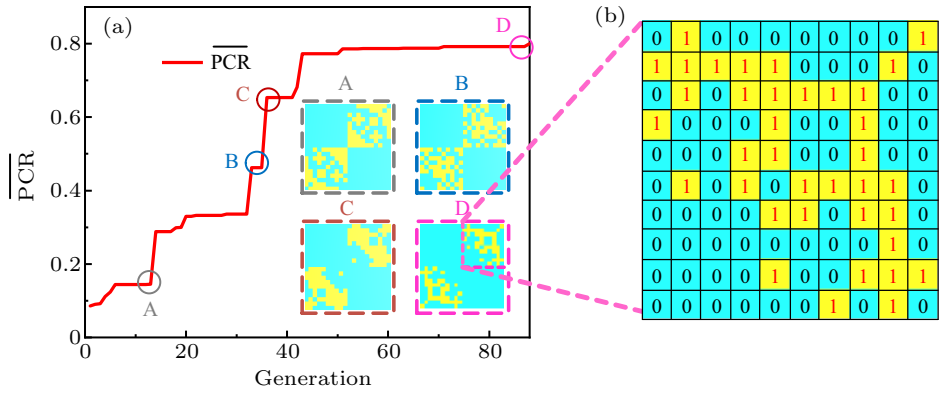


Fig. 4. (a) Relationship between the change of fitness function and the number of iterations during genetic optimization and the evolution of intermediate topological metal patterns. (b) Schematic representation of the coding sequence in the first quadrant of D.

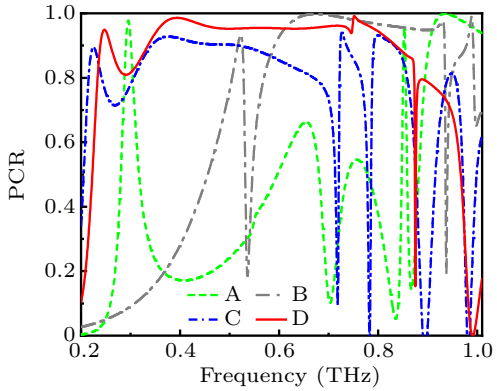


Fig. 5. Polarization conversion rate of quadrants A–D during genetic algorithm optimization; the incident angle is 45°.

To compare more intuitively the polarization conversion rates and relative operating bandwidths in different cases during the optimization process, the polarization conversion rates of A–D are analyzed, with the incident angle at 45° being evaluated when the PCR is more than 80%. The results are shown in Fig. 5. From the figure, it can be seen that from A to D there is a gradual and progressive increase in the continuous relative bandwidth. After calculating the relative bandwidths as 26%, 49%, 95% and 117%, respectively, the final result has a relative operating bandwidth of about 4.5 times that at the beginning of the iteration. This verifies the validity of the evolutionary process of topological metal pattern layers and structural parameters towards the optimal solution during the genetic algorithm optimization process.

4.1. Performance of the polarization converter

As the proposed polarization conversion unit is symmetric along the diagonal direction, so $r_{xy} = r_{yx}$ and $r_{yy} = r_{xx}$. Firstly, the case of vertically incident y-polarized waves is in-

vestigated. The reflection spectra are obtained by frequency-domain simulations, as shown in Fig. 6(a). From this figure, it can be observed that within the frequency range 0.231–0.995 THz, the cross-polarization reflection coefficient r_{xy} is greater than 0.9, while the co-polarization reflection coefficient r_{yy} is less than 0.3. This indicates that the incident y-polarized waves are converted into x-polarized waves reflecting from the metasurface. Subsequently, the PCR for the corresponding frequency range is calculated, as depicted in Fig. 6(b). The metasurface converter possesses a polarization conversion efficiency ratio higher than 0.9 and a relative bandwidth ratio of 125% in the 0.231–0.995 THz range, which indicates excellent polarization conversion performance.

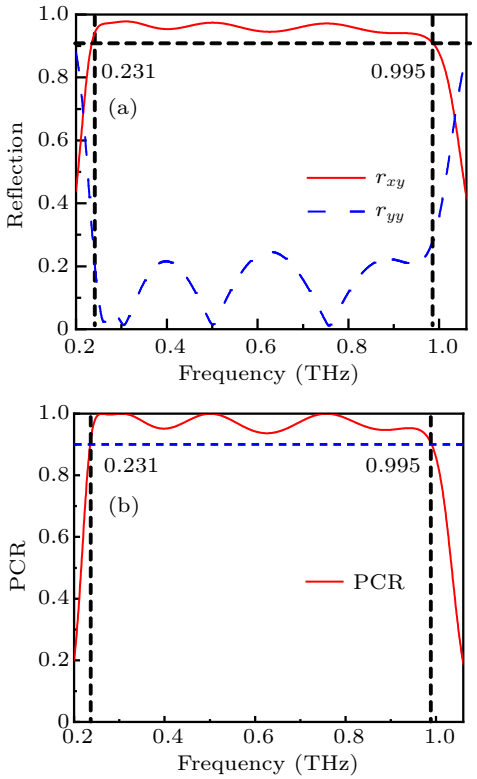


Fig. 6. (a) Reflectivity of co and cross-polarized for x and y polarized waves. (b) PCR of the topologically optimized polarization conversion metasurface.

To describe the state of reflected THz waves more accurately, the Stokes coefficients for a reflective hypersurface[6] are derived from Stokes' formulae and are represented by the following equations:

$$S_0 = r_{xy}^2 + r_{yy}^2, \tag{5}$$

$$S_1 = r_{yy}^2 - r_{xy}^2, \tag{6}$$

$$S_2 = 2\left|r_{yy}\right|\left|r_{xy}\right|\cos\varphi_{\text{diff}}, \tag{7}$$

$$S_3 = 2\left|r_{yy}\right|\left|r_{xy}\right|\sin\varphi_{\text{diff}}, \tag{8}$$

where φ_{diff} denotes the phase difference between the y-polarized to x-polarized and y-polarized to y-polarized reflected THz waves. Figure 7(a) depicts the polarization ellipsoid of the reflected THz wave, where χ and ψ denote the ellipticity angle and polarization rotation angle of the reflected THz wave, which satisfy $\sin(2\chi) = S_3/S_0$ and $\tan(2\psi) = S_2/S_1$, respectively.

We investigated the ellipticity angle and polarization rotation angle of the reflected THz wave as a function of frequency. The results are shown in Fig. 7(b), where the black dashed line indicates the ellipticity angle χ and the red solid line indicates the polarization rotation angle ψ. It can be seen that at 0.231–0.995 THz the ellipticity angle χ is in the range of $-0.89°$ to $0.93°$, which is close to $0°$. At 0.231–0.995 THz, the polarization rotation angle ψ is about $\pm 89.5°$, which is close to $90°$. This means that the incident y-polarized wave is converted into an almost pure x-polarized wave, which has high linear polarization in the broadband range.

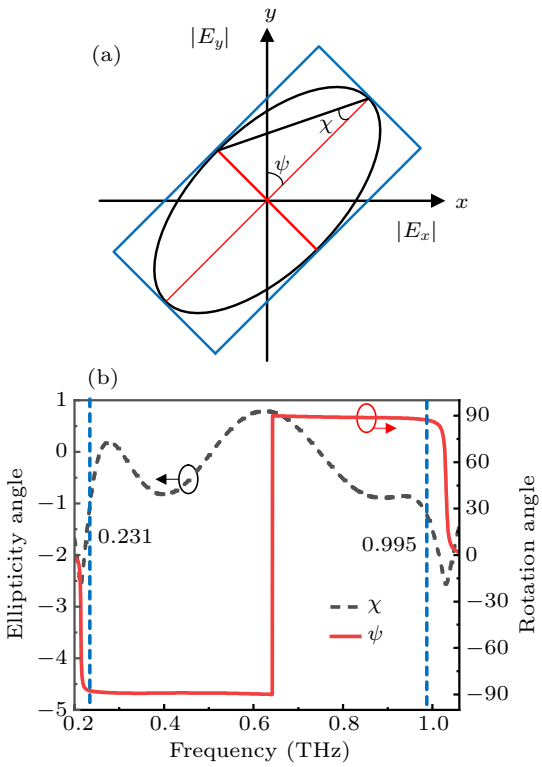


Fig. 7. (a) Polarized ellipsoid of a THz wave reflected by the polarization converter. (b) Polarization rotation angle ψ and ellipticity angle χ for y-polarized normal incidence.

4.2. Analysis of the polarization converter

To explain the ultra-wideband polarization conversion characteristics of the designed metasurface, the incident and reflected electric fields of the metasurface unit are decomposed along the u–v axes, as shown in Fig. 8(a). THz waves in the u and v directions are simulated, and the reflection coefficients and phase difference $\Delta\varphi$ between the u and v directions are obtained, as shown in Fig. 8(b). From the figure, it can be observed that within the frequency range 0.231–0.995 THz, the reflection coefficients r_u and r_v are approximately equal in the range of 0.92–0.98 and the phase differences $\Delta\varphi$ are

$180° \pm 30°$,[16,29] which are considered acceptable for cross-polarization convention. Therefore, based on the theoretical analysis of linear polarization conversion mentioned earlier, after being reflected by the metasurface the electric field direction along the u or v direction will reverse. As a result, the direction of the synthesized electric field will deviate by 90° from the y direction to the x direction, thereby achieving ultra-wideband polarization conversion.

To further analyze the mechanism of ultra-wideband polarization conversion achieved by the designed metasurface, the surface currents at four resonant frequency points of 0.313 THz, 0.488 THz, 0.778 THz and 0.943 THz in Fig. 6(a) are simulated, as shown in Fig. 9. The red arrows represent the direction of surface currents on the metallic pattern layer, while the black arrows represent the direction of surface currents on the metallic substrate. At 0.313 THz, it can be observed that the surface currents on the metallic pattern layer and the metallic substrate are in opposite directions, forming an equivalent magnetic resonator. At 0.488 THz, the surface currents on the metallic pattern layer and the metallic substrate are in the same direction, forming an equivalent electric resonator. At 0.778 THz, the surface currents on the metallic substrate are directed towards the lower left, while near the central and edge positions of the metallic pattern layer they are along the upper right and lower left. This indicates the simultaneous presence of magnetic and electric resonances. Similarly, at 0.943 THz, both electric and magnetic resonances are observed. Due to the resonance enhancement of electric and magnetic fields within the frequency range of 0.231–0.995 THz, ultra-wideband polarization conversion is achieved.

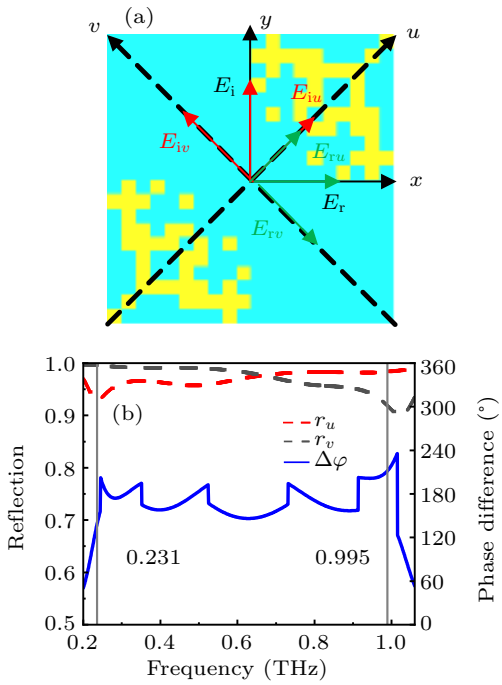


Fig. 8. (a) Operating principle of polarization conversion. (b) Reflected amplitude and phase difference of the reflected wave along the u and v directions.

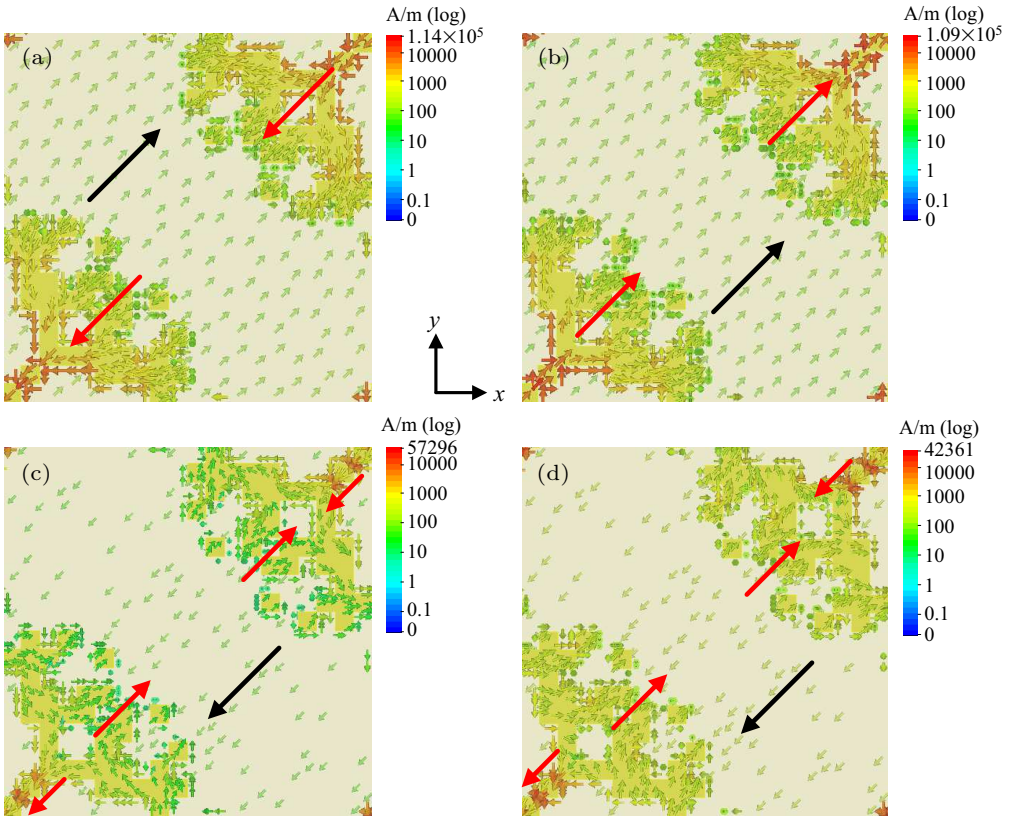


Fig. 9. Current distribution on upper and lower metal surfaces: (a) 0.313 THz, (b) 0.488 THz, (c) 0.778 THz, (d) 0.943 THz.

4.3. The effect of incident angle and polarization angle

The wide-angle characteristic of THz polarization conversion devices is crucial in practical engineering applications. Therefore, we investigate the dependence of polarization conversion efficiency on incident angle and polarization angle.

Firstly, the dependence of the polarization conversion efficiency of topologically optimized metasurfaces on the incident angle θ is investigated. The PCR curves with varying frequencies for incident angles of 0°, 15°, 30° and 45° are shown in Fig. 10. From the figure, it can be observed that within the range 0°–15° the PCR remains above 90% throughout the operating frequency band, exhibiting a polarization conversion efficiency consistent with that of vertical incidence. When the incidence angle is 30°, a narrow resonance peak appears at 0.964 THz, the converter also possesses a PCR higher than 90% and a bandwidth ratio of 123% in the range of 0.231–0.964 THz. When the incidence angle is 45°, the PCR remains above 80% in the range of 0.231–0.876 THz, and the relative bandwidth is 117%. Therefore, in the range of incident angles from 0° to 45°, the reduction in relative bandwidth with increasing incident angle is relatively small, indicating good wide-angle characteristics.

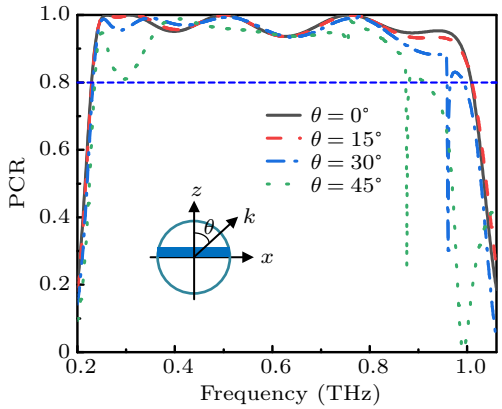


Fig. 10. Metasurface conversion efficiency versus angle of incidence.

In practical applications, there may be deviations in the polarization angle of electromagnetic waves that can have a certain impact on the polarization conversion of metasurfaces. The dependence of the polarization conversion rate on the polarization angle of the incident wave was investigated, as shown in Fig. 11. In this figure, it can be observed that when the polarization angle ϕ is within the range of $-10°$ to 10°, the PCR values of the metasurface remain above 85% throughout the operating frequency band and the relative bandwidth remains almost unchanged. Similarly, when the polarization angles ϕ are 15° and $-15°$, the PCR values of the metasurface remain around 80% throughout the operating frequency band. Therefore, within the range of polarization angles from $-15°$ to 15°, the dependence of the polarization conversion efficiency of the metasurface on the polarization angle is relatively low.

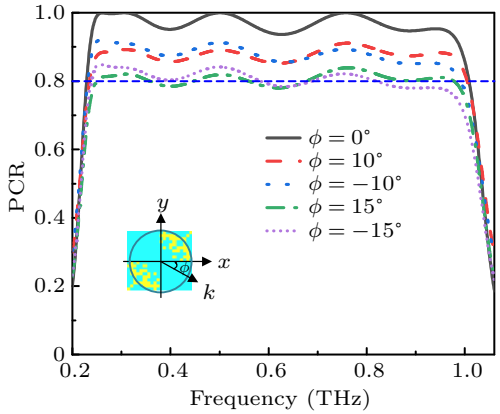


Fig. 11. Metasurface conversion efficiency versus polarization angle.

Table 2 presents a comparison between the structure proposed in this paper and reported broadband polarization converters for THz waves, where the maximum angle of incidence and polarization were evaluated when the PCR was more than 80%. The proposed structure has superior performance compared with other reflective linear polarization conversion metasurfaces. The structures proposed in Refs. [16–18] have the highest PCR values of 95% or 99% in the operating bandwidth range, but the relative bandwidths of the structures are all less than 83%. The dual-split-ring structure proposed in Ref. [15] can achieve a similar PCR value and relative operating bandwidth as this work, but the incidence angle feature is only 20°. In summary, it can be seen that the proposed reflective THz linear polarization conversion metasurface has the large relative operating bandwidth as well as good wide-angle characteristics.

Table 2. Comparison with other THz band broadband polarization converters.

Reference	Design technique (resonators)	Working bandwidth (THz)	Relative bandwidth (%)	PCR (%)	Incident angle feature (°)	Polarization angle feature (°)
[13]	T-shaped	0.31–1.05	102	80	45	–
[14]	crescent-shaped	0.64–1.47	79	90	30	–
[15]	dual-split-ring	0.49–1.88	117	90	20	10
[16]	dumbbell-shaped	1.76–4.26	83	95	40	–
[17]	C- and T-shaped	5–10	67	99	30	–
[18]	all dielectric	1.21–1.92	45	95	–	–
[25]	circular split-ring	0.912–2.146	81	90	40	10
This work	topological design	0.231–0.995	125	90	45	15

5. Conclusion and perspectives

In this paper, we utilized the topological optimization method to inversely design a reflective THz linear polarization conversion metasurface with wide-angle and ultra-broadband characteristics. Simulation results demonstrate that under vertical plane wave incidence, in the frequency range of 0.231–0.995 THz, the metasurface achieves a PCR exceeding 90% and the relative bandwidth is 125%. Furthermore, the physical mechanism underlying the realization of ultra-wideband polarization conversion is explained through theoretical analysis of linear polarization conversion and the surface current distribution. When the angle of incidence ranges from 0° to 45° and the polarization angle from −15° to 15°, the PCR remains above 80%, and the operational bandwidth with high polarization conversion efficiency varies minimally. Valuable references are provided for the design of wide-angle broadband polarization conversion devices in the THz band, and the proposed metasurface has potential applications in THz polarization imaging, communication and spectral detection fields.

Data availability statement

Data underlying the results presented in this paper are not publicly available at this time but may be obtained from the authors upon reasonable request.

Acknowledgements

Project supported by the National Natural Science Foundation of China and the Open Project Program of Wuhan National Laboratory for Optoelectronics (Grant No. 2022WNLOKF012).

References

[1] Kutas M, Haase B, Bickert P, Riexinger F, Molter D and von Freymann G 2020 *Science Advances* **6** eaaz8065
[2] Nagatsuma T, Ducournau G and Renaud C C 2016 *Nat. Photon.* **10** 371
[3] Mittleman D M 2018 *Opt. Express* **26** 9417
[4] Xu S T, Fan F, Ji Y Y and Chang S J 2021 *Opt. Express* **29** 8824
[5] Ako R T, Lee W S L, Atakaramians S, Bhaskaran M, Sriram S and Withayachumnankul W 2020 *APL Photon.* **5** 046101
[6] Jing X F, Gui X C, Zhou P W and Hong Z 2018 *J. Lightwave Technol.* **36** 2322
[7] Zhang Y H, Luan W M, Yan X N, Gao X Z, Zeng X D, Jin Z M, Ma G H and Yao J Q 2022 *Appl. Phys. B* **128** 156
[8] Cheng Y Z, Gong R Z and Wu L 2017 *Plasmonics* **12** 1113
[9] Zhou Q G, Li Y, Li Y Z, Yao N J and Huang Z M 2023 *Chin. Phys. B* **32** 024201
[10] Qi Y P, Zhang B H, Liu C Q and Deng X Y 2020 *IEEE Access* **8** 116675
[11] Xi Y, Jiang W, Hong T, Wei K and Gong S X 2021 *Opt. Express* **29** 22427
[12] Xu H X, Hu G W, Wang Y Z, Wang C H, Wang M Z, Wang S J, Huang Y J, Genevet P, Huang W and Qiu C W 2021 *Light: Sci. Appl.* **10** 75
[13] Ako R T, Lee W S L, Bhaskaran M, Sriram S and Withayachumnankul W 2019 *APL Photon.* **4** 096104
[14] Gandhi C, Babu P R and Senthilnathan K 2019 *Journal of Infrared, Millimeter, and Terahertz Waves* **40** 500
[15] Xu Z H, Sheng H Y, Wang Q L, Zhou L P and Shen Y C 2021 *SN Applied Sciences* **3** 763
[16] Nagini K B S S and C D S 2022 *IEEE Photonics Journal* **14** 1
[17] Bai J J, Chen T T, Wang S S, Xu W and Chang S J 2023 *Appl. Phys. A* **129** 610
[18] Zhao J C, Li N and Cheng Y Z 2023 *Opt. Commun.* **536** 129372
[19] Zhao J X, Song J L, Zhou Y, Liu Y C and Zhou J H 2020 *Chin. Phys. Lett.* **37** 064204
[20] Li J S and Li X J 2022 *Opt. Express* **30** 12823
[21] Li Z W and Li J S 2021 *Appl. Opt.* **60** 2450
[22] Zhuang L Y, Zhang W J, Chao M H, Liu Q S, Cheng B, Song G F and Liu J T 2024 *Opt. Mater. Express* **14** 483
[23] Du H T, Jiang M Z, Zeng L Z, Zhang L H, Xu W L, Zhang X W and Hu F R 2022 *Chin. Phys. B* **31** 064210
[24] Yu F Y, Wang Q C, He M X, Shen X B, Meng D S, Zhu J B and Wen Q Y 2023 *Euro. Phys. J. D* **77** 82
[25] Yan D X, Feng Q Y, Yuan Z W, Meng M, Li X J, Qiu G H and Li J N 2022 *Chin. Phys. B* **31** 014211
[26] Li N C, Mei J S, Gong D G and Shi Y C 2022 *Opt. Commun.* **521** 128581
[27] Sui S, Ma H, Wang J F, Feng M D, Pang Y Q, Xia S, Xu Z and Qu S B 2016 *Appl. Phys. Lett.* **109** 014104
[28] Borgese M, Costa F, Genovesi S, Monorchio A and Manara G 2018 *Scientific Reports* **8** 7651
[29] C D S and Karthikeyan S S 2019 *IEEE Transactions on Antennas and Propagation* **67** 2819